Nanoscale

PAPER

View Article Online
View Journal | View Issue

Cite this: *Nanoscale*, 2023, **15**, 15686

Functionalized manganese iron oxide nanoparticles: a dual potential magneto-chemotherapeutic cargo in a 3D breast cancer model†

Satish S. Phalake, [a] Sandeep B. Somvanshi, [b,c] Syed A. M. Tofail,[d] Nanasaheb D. Thorat *[d,e] and Vishwajeet M. Khot *[a]

Localized heat generation from manganese iron oxide nanoparticles (MIONPs) conjugated with chemotherapeutics under the exposure of an alternating magnetic field (magneto-chemotherapy) can revolutionize targeted breast cancer therapy. On the other hand, the lack of precise control of local temperature and adequate MIONP distribution in laboratory settings using the conventional two-dimensional (2D) cellular models has limited its further translation in tumor sites. Our current study explored advanced 3D *in vitro* tumor models as a promising alternative to replicate the complete range of tumor characteristics. Specifically, we have focused on investigating the effectiveness of MIONP-based magneto-chemotherapy (MCT) as an anticancer treatment in a 3D breast cancer model. To achieve this, chitosan-coated MIONPs (CS–MIONPs) are synthesized and functionalized with an anticancer drug (doxorubicin) and a tumor-targeting aptamer (AS1411). CS–MIONPs with a crystallite size of 16.88 nm and a specific absorption rate (SAR) of 181.48 W g^{-1} are reported. *In vitro* assessment of MCF-7 breast cancer cell lines in 2D and 3D cell cultures demonstrated anticancer activity. In the 2D and 3D cancer models, the MIONP-mediated MCT reduced cancer cell viability to about 71.48% and 92.2%, respectively. On the other hand, MIONP-mediated MCT under an AC magnetic field diminished spheroids' viability to 83.76 ± 2%, being the most promising therapeutic modality against breast cancer.

Received 13th June 2023,
Accepted 5th September 2023

DOI: 10.1039/d3nr02816j

rsc.li/nanoscale

1. Introduction

The future of magnetic nanoparticles' (MNPs) use in applications such as heat-mediated drug delivery, catalysis, self-heating materials, magnetic fluid hyperthermia (MFH) therapies,[1] MRI-guided drug delivery,[2] and heat-triggered remote biological process control may depend on the enhancement of the heating effectiveness of MNPs under alternating magnetic fields (AMFs).[3,4] It is projected that 297 790 women and 2800 men will be diagnosed with invasive breast cancer in the USA in 2023, and another 55 720 women will be found to have ductal carcinoma *in situ* (DCIS). In the year 2023, approximately 43 700 lives will be lost due to breast cancer, with 43 170 of those deaths affecting women and 530 impacting men.[5] Targeted heating of cancerous tumors to temperatures between 42.0 to 44.0 °C, known as hyperthermia, is an alternative strategy for treating cancer. This method either causes direct cell death or makes the tumor more receptive to chemotherapy or radiation therapy. To ensure the safety of MFH, we optimized the parameters of the AMF by selecting a low frequency (f) and an appropriate strength of the AMF. This optimization aimed to minimize exposure times while maintaining bio-safety. Magnetic hyperthermia therapy (MHT) utilizes MNPs to generate heat after exposure to an AMF. This heat is then used to selectively treat specific tumor tissues while minimizing damage to surrounding normal tissues, as it avoids significant overall temperature elevation.[6,7] Due to their superior magnetic properties, excellent biocompatibility, and

[a]*Department of Medical Physics, Centre for Interdisciplinary Research, D. Y. Patil Education Society (Deemed to be University), Kolhapur, 416 006 Maharashtra, India. E-mail: wish.khot@gmail.com*
[b]*School of Materials Engineering, Purdue University, West Lafayette, USA*
[c]*Department of Physics, Dr. B. A. M. University, Aurangabad-431004, Maharashtra, India*
[d]*Department of Physics and Bernal Institute, Limerick Digital Cancer Research Centre (LDCRC), University of Limerick, Castletroy, Co. Limerick, Limerick, V94 T9PX, Ireland. E-mail: nanasaheb.d.thorat@ul.ie*
[e]*Nuffield Department of Women's and Reproductive Health, John Radcliffe Hospital, Medical Sciences Division, University of Oxford, Oxford OX3 9DU, UK. E-mail: thoratnd@gmail.com*

†Electronic supplementary information (ESI) available: Additional details of the energy dispersive X-ray analysis (EDX) and the details of induction heating, *i.e.* slope values calculated from the temperature *versus* time plot and SAR values of the different concentrations of nanoparticles under an AMF of appropriate field strength. See DOI: https://doi.org/10.1039/d3nr02816j

biodegradability, magnetite-based MNPs have recently been recognized as promising candidates for bio-applications. In fact, the Food and Drug Administration (FDA) has already permitted the use of several products of magnetite-based NPs in humans.[8] Over the past twenty years, there has been an addition of newly developed synthetic nanomaterials that have emerged and been utilized in the field of biomedicine, specifically in the context of cancer treatment. Many synthetic functional nanomaterials have been created and are currently being used in the biomedical field, most notably for the treatment of cancer. A recently emerged method on the basis of nanotechnology is projected in the oncological field to better effectively treat cancer tumors: magneto-chemotherapy (magnetic hyperthermia + chemotherapy).[9] Meanwhile, a new aspect of magneto-chemotherapy has opened up with the development of MNP-based MFH therapy.[10]

Chemical co-precipitation is one of the most straightforward processes for synthesizing MNPs in an aqueous solution. Various synthesis factors can be changed, including concentration, pH, temperature, and particle size. The particle size distribution, shapes, and formulations of MNPs affect their specific absorption rate (SAR); when subjected to an AMF, this may result in insufficient heat generation to effectively eliminate the targeted tumor cells.[8] A range of surfactants were used for a coating to maintain the colloidal properties and biocompatibility of manganese iron oxide nanoparticles (MIONPs) and prevent aggregation caused by magnetic dipole–dipole interactions. These surfactants encompass both polymeric and non-polymeric substances, including lipids and proteins. MIONPs are coated with different polymers, such as chitosan (CS), oleic acid, starch, pullulan, dextran, and others, to make them suitable for *in vivo* applications. Among these is CS, a substance with unique characteristics like bio-compatibility, bio-degradability, film-forming potential, and bio-adhesion, which has received much attention regarding biodegradability and toxicity. CS offers the advantage of having aminated groups, which present a variety of active sites for additional biofunctionalization. This characteristic of CS provides further benefits. When MIONPs are exposed to an AMF, localized heating is generated, specifically within the tumor tissues. Unfortunately, its use in the biomedical area has been constrained by the absence of an exact heating range and appropriate MIONPs distribution in an *in vivo* environment. An alternative to *in vivo* models is to evaluate *in vitro* tumor models. The commonly employed two-dimensional (2D) *in vitro* models, however, cannot accurately represent all the properties of a patient's tumor and, as a result, cannot create details of the experimentally important parameters and issues.[8]

Three-dimensional (3D) cell culture models are basic constructs that better imitate the composition and structure of tumors. These models offer a more authentic environment for assessing cellular reactions to treatments. Furthermore, 3D cell culture models enable the creation of numerous identical copies, serving as a viable alternative for conducting initial tests before *in vivo* experiments, thereby helping to reduce the required number of animals.[11] As 3D tumor models are proven to be the most accurate representation of *in vivo* conditions for various cell types in laboratory settings, conducting magnetic hyperthermia combined with chemotherapy (MHCT) studies using these models allows for greater clinical relevance. This enables the detailed investigation of magnetic parameter optimization, distribution of MIONPs, heating dissipation, therapeutic effects, and the development of thermotolerance in cancer cells.[12] According to recent numerical simulations using 3D realistic human body models, it has been found that the magnetic field amplitude (*i.e.*, $H \times f$) can reach values that are up to four times higher than the generally accepted safety value of 5×10^8 A m^{-1} s^{-1} and still be considered acceptable. Another essential task is reducing the concentration of MIONPs necessary for successful therapy. Due to their excellent biocompatibility and stability, MIONPs are unquestionably the most practical building blocks for MHT in this regard.[13]

This report provides a practical approach for creating well-defined, high magnetic moments of MIONPs and surfaces modified with chitosan. Through an electrostatic linkage, the anticancer drug doxorubicin (DOX) is attached. DOX is being utilized as a representative anti-tumor drug to assess the loading and *in vitro* drug-releasing properties of chitosan-coated magnetic nanoparticles in sustained and triggered release modes. Aptamers, derived from the Latin words "Aptus" or "Aptare," refer to nucleotide polymers with a remarkable ability to precisely and tightly bind to target molecules. However, the unique strengths of aptamers have recently posed a challenge to the role of antibodies in both *in vitro* diagnostics and drug therapy. Nucleic acid aptamers were discovered through techniques like exponential enrichment ligand phylogenetic technology. Additionally, aptamers offer the benefits of facile modification or attachment of functional groups, potent tissue penetration, robust thermal and chemical stability, and low immunogenicity.[14] Aptamers have some advantages over antibodies as tumor-targeting ligands, including minimal immunogenicity and reasonable binding specificity. Due to their high affinity and high specificity, aptamers (AS1411), a class of small single-stranded DNAs (ssDNA) that fold into a secondary or tertiary structure, are commonly known to be practical tools for binding target molecules.[15,16] Selected aptamers demonstrated strong selectivity towards particular entities, including proteins, peptides, and whole-cell attachments. However, most aptamers are highly susceptible to *in vivo* nuclease destruction, do not penetrate the cell, and need intricate surface alterations to join other medications or carriers.[17] The cytotoxicity and anticancer capabilities of CS–MIONPs were evaluated using MCF-7 cell lines in 2D and 3D cell culture systems. The utilization of 3D models allows for conducting magneto-chemotherapy (MCT) analysis with increased clinical significance, enabling comprehensive investigations of magnetic parameter optimization, distribution of MIONPs, heat dissipation, therapeutic effects, and the development of acquired thermotolerance in cancer cells. These 3D models have demonstrated their ability to faithfully

replicate *in vivo* conditions, enhancing the accuracy and applicability of MCT investigations.

2. Experimental details

2.1 Reagents and method

The materials iron(III) chloride ($FeCl_3$) ≥ 99%, iron(II) chloride ($FeCl_2$) ≥ 99%, manganese(II) chloride ($MnCl_2$) ≥ 99%, sodium hydroxide (NaOH) ≥ 99%, hydrochloric acid (HCl), acetic acid, chitosan, aptamer (AS1411), and doxorubicin hydrochloride (DOX·HCl) were all acquired from Sigma-Aldrich and used to synthesize MIONPs. All reagents were utilized without any additional modifications. In a typical synthesis of MIONPs, iron(III) chloride (2 mmol), manganese(II) chloride (0.750 mmol), and iron(II) chloride tetrahydrate (0.250 mmol) were individually dissolved in deionized water (DW) while maintaining continuous stirring. The resulting solution was then precipitated with NaOH, added directly, and maintained at 70 °C to 80 °C for two hours until co-precipitation occurred at pH 12.[18] The precipitation of the MIONPs formed according to the following reaction:

$$0.75Mn^{2+} + (0.25)Fe^{2+} + 2Fe^{3+} + 8OH^- \rightarrow 0.75Mn(OH)_2 \cdot (2.25)Fe(OH)_6$$

$$0.75Mn(OH)_2 \cdot (2.25)Fe(OH)_6 \rightarrow Mn_{0.75}Fe_{2.25}O_4 + 4H_2O.$$

The precipitate was recovered by magnetic decantation and double-distilled water was used to wash it away. The cleaned precipitate was dried at room temperature.

2.2 Surface modification of MIONPs with chitosan (CS–MIONPs)

For the coating process, uncoated MIONPs were utilized. A solution of 1% (w/v) chitosan (CS) in 2% (v/v) acetic acid was employed to dissolve 1% of the bare MIONPs. After 30 minutes, the mixture was subjected to ultrasonication. The CS–MIONPs were ultrasonically cleaned, and then allowed to settle before being washed three times with distilled water to eliminate any extra CS. Following their separation, CS–MIONPs were dried in air at 50 °C. The procedure steps are shown in Fig. S1 (ESI†).[18]

To conjugate the anticancer drug doxorubicin (DOX) with CS–MIONPs, EDC/NHS coupling chemistry was employed. In the initial step, 1.00 mg of DOX was dissolved in 1 mL of DW. Subsequently, a solution containing 0.500 mg of EDC and 1 mg of NHS was gradually added drop by drop to the DOX solution. The resulting mixed solution was kept on a stirrer at 4 °C for a whole night. Following this, the precursor solution was combined with a 20 mg CS–MIONP solution in 10 mL of DW, and the resulting solution was continuously stirred in the dark at 4 °C for an additional 24 hours. The DOX-encapsulated nanoparticles were then magnetically separated and rinsed with DW. The particles were subsequently dispersed in 1.00 mL of DW at a concentration of 1 mg mL^{-1}. UV absorbance measurements were conducted on the hybrid suspension to assess the doxorubicin loading onto the CS–MIONPs directly. The absorbance studies were conducted by UV-Vis spectroscopy. The absorbance at 480 nm was recorded to determine the doxorubicin quantity. Fluorescence measurements were carried out to assess the loading effectiveness. The DOX-releasing behavior of DOX from the CS–MIONP micelle was studied under various pH conditions in DW.

For AS1411 aptamer modification, a solution of PEG–DOX@CS–MIONP nano complex (2 mL) was prepared, and 1 mg of EDC was dissolved in it, followed by incubation at 37 °C for 15 minutes. After that, 1 mg of NHS and 20 mL of 250 mM AS1411 aptamer were introduced, and the reaction was continued at 37 °C for 2 hours. The resulting mixture was then subjected to centrifugation, followed by washing with water. The resulting precipitate was dispersed in 2 mL of PBS for subsequent use.[19]

2.3 Structural and magnetic characterizations

The powder XRD patterns were used to identify the structure of the MIONPs by employing a miniflex 600 diffractometer with Cu Kα (λ = 1.5406 Å) radiation. Fourier transform infrared (FT-IR) spectroscopy (Bruker alpha (II) unit) was employed to confirm the cubic spinel phase and examine the surfactant ligands. The morphological characterization studies were performed by transmission electron microscopy (TEM) with a JEOL JEM-2100 microscope operating at 200 kV, and an EDXS (energy-dispersive X-ray spectroscopy) detector was used for composition studies. The thermal stability of the particles, surfactant decomposition temperature, and quantification of the surfactant ligands were determined using thermogravimetric analysis and differential scanning calorimetry. The colloidal stability was assessed by determining the zeta potential using Malvern Instruments. Magnetic studies were performed at 300 K with an applied field of ±15 kOe using a Lake Shore 7400 Series vibrating sample magnetometer (VSM).

2.4 Magnetic hyperthermia experiments

To perform the induction heating of the prepared nanoparticles in a physiological medium, an Easy Heat 8310 system (Ambrell, UK) was employed. A 60 mm diameter coil consisting of 3 turns was utilized for this purpose. The effectiveness of the nanoparticles for MHT was assessed using temperature profile curves, with a frequency of 277 kHz and an AMF amplitude ranging from 13.3 kA m^{-1} to 26.7 kA m^{-1}.

2.5 *In vitro* drug release in cancer cells

A total of 1×10^5 MCF7 cells were seeded in a μ-Dish 35 mm and allowed to incubate for 24 hours. Subsequently, either the control sample (only DOX at a concentration of 1 μg mL^{-1}) or CS–MIONPs loaded with DOX at a concentration of 100 μg mL^{-1} were used as the growth medium. After an additional 4 and 24 hours of culture, the cells were rinsed three times with PBS. After the rinsing, the cells were fixed with 4% formaldehyde in PBS for 20 minutes and then cleaned three times with PBS. To assess the delivery of DOX, the cell nuclei of MCF7 cells were stained with 10 μL of DAPI (10 mM) for 10 minutes. The cells were washed three times with PBS and

the dishes were observed using a LEICA TCS SP5 confocal microscope (Leica Microsystems, Germany). DAPI fluorescence was visualized using an excitation wavelength of 405 nm, while DOX fluorescence was visualized upon excitation at 511 nm. High-magnification images of MCF7 cells were captured using a 40× oil-immersion lens.

2.6 *In vitro* anticancer activity

MCF7 cells were seeded in a 96-well plate at a density of 1×10^5 cells per well. After the initial 24 hours of incubation, the cell culture medium was replaced with a fresh mixture containing different concentrations of DOX-loaded CS–MIONPs and free DOX. The cells were then incubated for an additional 24 hours before the MTT experiment. In brief, the cell culture medium was aspirated and MTT in FBS-free DMEM (10 mM) was added. After an additional 3 hours of incubation, the MTT solution was removed, and 100 μL of DMSO was added to dissolve the formazan crystals that had formed. The cell viability was subsequently determined by measuring the absorbance at 570 nm. The experiments were repeated three times and the mean and standard deviation (SD) of the data were presented graphically. The relative cell viability (%) compared to the control well containing the cells without the nanoparticles was calculated using the following equation:

$$[A_{\text{absorbance}}]_{\text{tested}}/[A_{\text{absorbance}}]_{\text{control}} \times 100.$$

2.7 *In vitro* magneto-chemotherapy on cancer cells

In order to evaluate the effectiveness of *in vitro* magneto-chemotherapy, MCF7 cells were cultured with CS–MIONPs alone and DOX-loaded CS–MIONPs at a concentration of 1 mg mL^{-1} for 24 hours. The AC magnetic fields were kept activated until the upper limit of hyperthermia temperature, around 42–44 °C, was reached. The frequency applied for all *in vitro* experiments was 277 kHz and the AC magnetic field was maintained at 20 kA m^{-1}. In the center of the coil, media containing CS–MIONPs, DOX@CS–MIONPs and DOX@CS–MIONPs+Apt were suspended with 1 mL of cancer cells (2×10^5 cells per mL). The system was maintained at a constant temperature of 43–44 °C throughout the experiment, with a heating duration of 60 minutes provided by the samples containing nanoparticles and cells. The cells were immediately transferred to 96-well plates and cultured for an additional 24 hours. Simultaneously, the cell samples were cultured in slide Petri dishes with 2 mL of DMEM for subsequent confocal microscopy imaging after labeling with propidium iodide (PI) and DAPI. The cell viability was assessed using the MTT assay.

3. Results and discussion

3.1 Structural and morphological analysis

The XRD patterns of the MIONPs and chitosan-coated MIONPs (CS–MIONPs) are shown in Fig. 1a. The characteristic broad diffraction peaks confirmed the crystalline nature for both the MIONPs and reflection planes (220, 311, 400, 422, 511, 440, and 622) indicate the presence of a cubic spinel structure, which matched with JCPDS card no. 19-0629. The crystallite size of the synthesized MIONPs was determined using the Debye–Scherrer relationship, which was determined to be 16.88 nm for the uncoated MIONPs and 13.91 nm for the CS–MIONP nanocomposite. The intensity decreased after capping the MIONPs with CS, and the peaks broadened, proving that the coating procedure reduced the particle size. The presence of an amorphous CS polymer coating on MIONPs could lead to a micro-strain, leading to peak broadening in the coated sample.[20]

Fig. 1b and 1c show the TEM images for both MIONPs and CS–MIONPs, and the corresponding histograms illustrate particle size distribution (inset). The TEM analysis of the MIONPs samples provides insights into the particle size and distribution, which align well with the results obtained from XRD analysis. The images reveal the presence of aggregated MIONPs in both spherical and irregular forms, with sizes of approximately $D = 20 \pm 0.15$ nm and $D = 13 \pm 0.20$ nm, as shown in Fig. 1b and 1c. The observed scattered ring patterns in the TEM images are in good agreement with the XRD analysis, showing a well-defined crystallite formation of the MIONPs. High-resolution TEM (HRTEM) images (Fig. S2(b and f), ESI†) exhibit lattice fringes at a spacing of approximately 0.270 nm, corresponding to the (311) plane, revealing the monophase formation. Fig. 1(b and c) demonstrates that the CS-coated MIONPs exhibit a nearly spherical shape and good dispersibility, with minimal agglomeration compared to the uncoated nanoparticles. Furthermore, the functionalization with CS molecules results in an increase in the average particle diameter. The non-magnetic nature of CS plays a significant role in reducing interparticle interactions, leading to improved dispersibility after coating. The crystalline formation of MIONPs is further supported by the corresponding SAED patterns in Fig. S2(c and g) (ESI†), which exhibit bright ring patterns. The corresponding planes, which are evidently visible in the XRD patterns, correspond to the ring motifs.[20] For a better understanding of the structure architecture of both samples, TEM-EDX chemical mapping was performed as shown in (Fig. 1f and 1g). TEM-EDX spectroscopy was used to further examine the chemical composition at the single-particle and few-particle cluster levels. Fe : Mn ratios were found for both the samples and a small cluster of particles, suggesting that the MIONPs have uniform chemical compositions. Table S1 (ESI†) provides a summary of the typical chemical compositions of the MIONPs used in this study. It demonstrates that with just slight deviations, the compositions of manganese(II) and iron(III) are essentially stoichiometric. By analyzing the EDX spectra of various macroscopic sections of the samples, the stoichiometric of the manganese and iron contents was evaluated.[21]

EDX was utilized to study the chemical composition of the synthesized MIONPs. The EDX spectra, presented in Fig. S3(a) (ESI†), verify the occurrence of all the desired elements in the MIONPs, and the corresponding analyzed results are depicted in the figure. The pure-phase nature of the MIONPs affirms

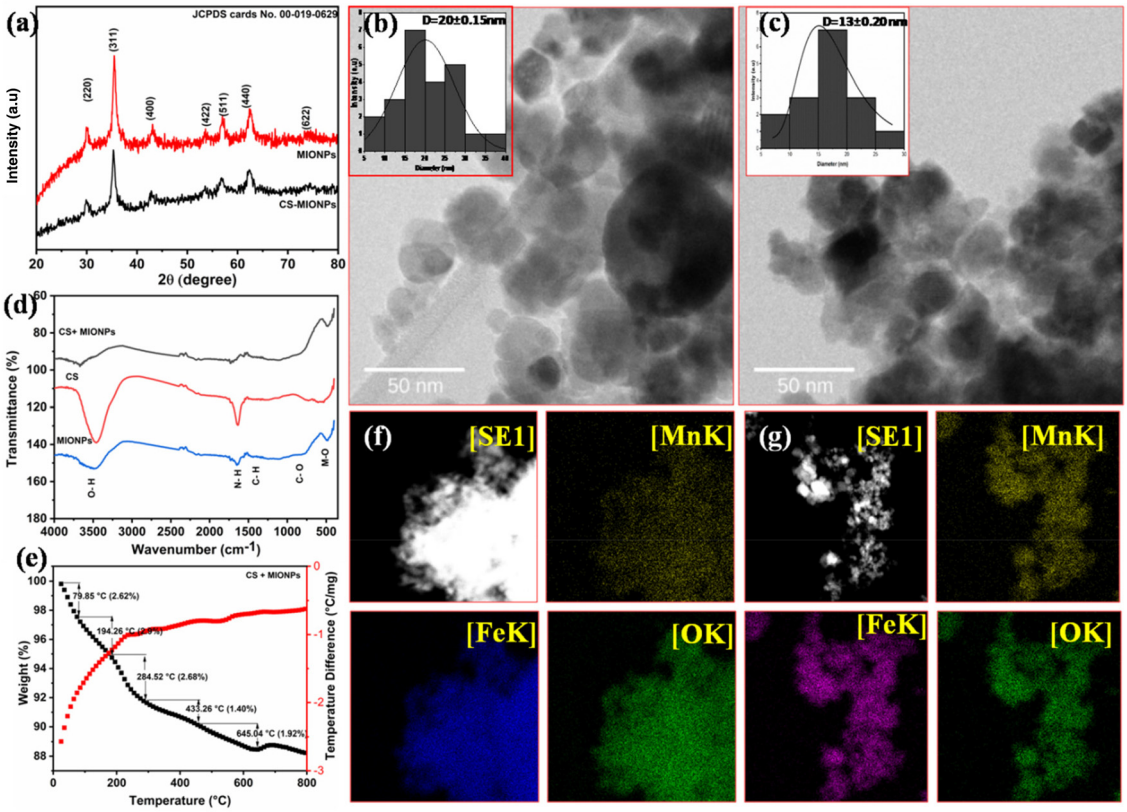

Fig. 1 (a) X-ray diffraction (XRD) patterns of the bare MIONPs and CS–MIONPs, (b and c) TEM image and histogram (inset) of the bare MIONPs and CS–MIONPs, (d) FT-IR spectra of the bare MIONPs, CS and CS–MIONPs. (e) Thermogravimetric spectra of the CS–MIONPs, and (f and g) TEM-EDX chemical mapping of the samples MIONPs and CS–MIONPs.

that they align with the desired compositional ratios, indicating that the stoichiometric preparation has been accurately sustained throughout the synthesis process.

The structural properties and bonding nature of the synthesized MIONPs and CS–MIONP nanocomposites were studied by infrared spectroscopy, and the FT-IR spectra of the bare MIONPs and CS–MIONPs along with CS are shown in Fig. 1f, respectively. The band detected at 455 cm^{-1} belongs to the Fe_{octa}–O vibrational bond at octahedral sites, while the band detected at 565 cm^{-1} belongs to the intrinsic Fe_{tetra}–O vibrational bond at the tetrahedral sites. When compared to the spectra of pure chitosan, the amide absorptions not only become stronger but also move to lower wavenumbers, such as 1630 cm^{-1}, which is indicative of hydrogen-bonded amides. The CH_2 group deformation is due to the sharp peak at 1400 cm^{-1}.[21] The peaks at 1620 and 3376 cm^{-1} are attributed to stretching (ν) vibrations of the –OH group and water adsorbed on the surfaces of the MIONPs, respectively. The main amino group ($-NH_2$) in CH forms strong hydrogen bonds with the oxygen in the MIONPs, as evidenced by the rise in absorption intensity at 1631 cm^{-1}.[22]

Thermogravimetric (TGA) curves and Differential Thermal Analysis (DTA) of the MIONPs Fig. S3(b) (ESI†) and CS–MIONPs are shown in Fig. 1e. The composition of the coating on the nanoparticles surface is further supported by quantitative data. The amount of oxidation of MIONPs decreased significantly as TG–DTA was carried out in an N_2 environment. The TGA experiments were designed to study the thermal stability of MIONPs and CS–MIONPs over the range of 50–800 °C. Depending on the reaction type, each thermogram had a different stage that corresponded to a different weight loss procedure. For all MIONP and CS–MIONP samples, a weight loss of 4% was noted below 110 °C due to the evaporation of physically adsorbed H_2O molecules. The weight loss in the last phase of the TGA plot belongs to the phase formation of MIONPs.[23] As a result, the simultaneous oxidation and the decomposition of CS molecules cause an exothermic peak to accumulate at 200–500 °C. The decomposition of chitosan molecules causes the other peak to appear at a temperature of around 160 °C. By analyzing the changes in the overall weight loss of the CS–MIONP samples, we can calculate the percentage of chitosan molecules that are bound to the surface of the nanoparticles. Based on this analysis, it was estimated that approximately 9% of the polymeric chitosan molecules are adsorbed onto the surface of the nanoparticles. Both samples achieve weight loss stability at temperatures above 600 °C. MNPs made up the majority of the remaining material after CS had completely broken down. The TGA curve showed how much CS was present in the CS–MIONPs.[24]

A magnetization study was performed to analyze how coating affects the magnetic characteristics of MIONPs and CS–MIONPs. The observed M_s value of the bare MIONPs was 51.06 emu g^{-1}, which was low compared to the theoretical value of the bulk MIONPs (M_s = 84 emu g^{-1}). Due to the finite size effect, M_s has been shown to diminish as MIONP particle sizes fall below 30 or 20 nm.[25,26] Fig. S3(c) (ESI†) shows the magnetization (*M*) *versus* field curves of the bare MIONPs and CS–MIONPs. In MIONPs and CS–MIONPs, coercivity and remanence are almost negligible based on VSM measurements. As seen in the figure, under an applied field of 15 kOe, the magnetization of the sample CS–MIONPs is lower (41.60 emu g^{-1}) than that of the sample MIONPs (51.06 emu g^{-1}). The magnetization of a magnetic material is directly influenced by its weight. Consequently, the magnetization decreases as chitosan is applied as a coating. The addition of organic coating layers, such as chitosan, to magnetic materials results in an increase in the proportion of the non-magnetic material, leading to a decrease in the overall magnetism of the material.[20,27]

As a result of Dynamic Light Scattering (DLS) measurements, the hydrodynamic diameter (HDD) and zeta potential (ξ) have been determined (Fig. S3(d–f), ESI†). The MIONP samples had an HDD of 362.1 nm, while the CS–MIONPs had an HDD of 645.7 nm. In previous studies, the MIONP content increased the hydrodynamic diameter of chitosan loaded with MIONPs. The dipole interface occurred from residual magnetic moments, and van der Waals forces may be responsible for this. They together may produce a particle size increase in magnetite nanoparticles.[28] The stability of CS–MIONPs was assessed by conducting zeta potential measurements under various conditions in water. When the zeta potential of the nanoparticles is measured, it can be used to determine the electrostatic interaction of the nanoparticles. During nanoparticle application in biomedicine, the zeta potential measurement is a crucial factor. The zeta potential of MIONPs is −20.4 mV and that of CS–MIONPs is −7.0 mV, respectively. The observed rise in positive zeta potential as the pH decreased is believed to be a result of the protonation of the free amino groups. This protonation process imparts a sufficient charge to ensure the stability of the coated nanoparticles. When the MIONPs are uniformly dispersed, the surface area of MIONPs is enhanced, which leads to enhanced heat transfer to the surrounding fluid. Compared to MIONPs that are not dispersed, a superior dispersion of MIONPs offers a comparable energy transfer. The HDD of MIONPs is smaller than that of CS–MIONPs.

3.2 Induction heating study

The inductive heat generation capability of MIONPs in the presence of an AC field was evaluated through the SAR, which quantifies the power of heat generated by the MIONPs per gram. The calculation of the SAR was performed using the following procedure:

$$\mathrm{SAR} = C\left(\frac{\mathrm{d}T}{\mathrm{d}t}\right)\left(\frac{M_s}{M_m}\right)$$

$$\mathrm{ILP} = \frac{\mathrm{SAR}}{fH^2}.$$

In this equation, *C* represents the specific heat capacity of the water, ($\mathrm{d}T/\mathrm{d}t$) is the initial rate of temperature change, M_m refers to the mass of dispersed MNPs, M_s represents the mass of the suspension, *H* represents the magnetic field, and *f* represents the frequency. The intrinsic loss power (ILP) parameter, which is the most suitable model, relies on the frequency and magnitude of the magnetic field, allowing for easy comparison across multiple tests. In Fig. 2c and 2d, typically the ILP value ranges from 0.2 to 9.9 nH m^2 g^{-1}, while MIONPs with lower ILP values may still be sufficient to heat in magnetic hyperthermia.[29] A higher SAR value is desirable as it corresponds inversely to M_m. From the perspective of SAR measurement, a positive control denotes a reference sample possessing the established and thoroughly defined electromagnetic absorption characteristics. Conversely, a negative control in the SAR measurement signifies a reference sample or condition exhibiting minimal to negligible electromagnetic absorption. In our study, MIONPs are the positive control, while water is the negative control for SAR measurement. The total power loss (*P*) comprises three mechanisms, *i.e.*, hysteresis losses, Néel relaxation losses, and Brownian relaxation losses.[30–32] Under AC magnetic fields, the capability of the CS–MIONPs sample to produce heat was evaluated. In this study, the magnetic heating experiments used a magnetic field for 10 minutes at a frequency of 277 kHz and an amplitude of H_{max} = 13.3–26.7 kA m^{-1}. The permissible limit for MHT is in the range of these parameters ($H_{max} \times f < 5 \times 10^9$ A m^{-1} s^{-1}).[33] CS–MIONPs serve as heating mediators that translate the AMF into thermal energy, leading to an increase in temperature. The environmental viscosity and the characteristics of MNPs, including their hydrodynamic size, saturation magnetization, and anisotropy, determine how much heat is dissipated during relaxation loss.[34] Fig. S4(a–e) and S5(a–e) (ESI†) illustrates the temporal temperature growth and SAR with their respective peak temperatures in an aqueous solution containing MIONPs and CS–MIONPs at dosages of 0.5, 1.0, 2.0, 5.0, and 10.0 mg ml^{-1}, at different AMF amplitudes ranging from 13.30 to 26.70 kA m^{-1}. It can be noted that the temperature difference increases with the AMF amplitude, as demonstrated in Fig. S6 (ESI†) for varying heating times. A linear correlation was observed between the AMF amplitude and the maximum temperature and the SAR. With a calculated SAR, the highest temperature rise within 10 minutes was the corresponding value.

According to the thermal response curves, the maximum temperature and SAR values increased as the strength of AMF intensified.[22] When the MIONPs dosage increases from 0.5 to 10.0 mg mL^{-1}, the estimated SAR value for the CS–MIONPs initially increases from 69.76 to 181.5 W g^{-1}. As the dosage increased, the SAR value decreased but remained higher than the values reported for $MnFe_2O_4$ MNPs prepared using other techniques.[33] The magnetic hyperthermia studies conducted on CS–MIONPs demonstrated the reliance of the SAR on the

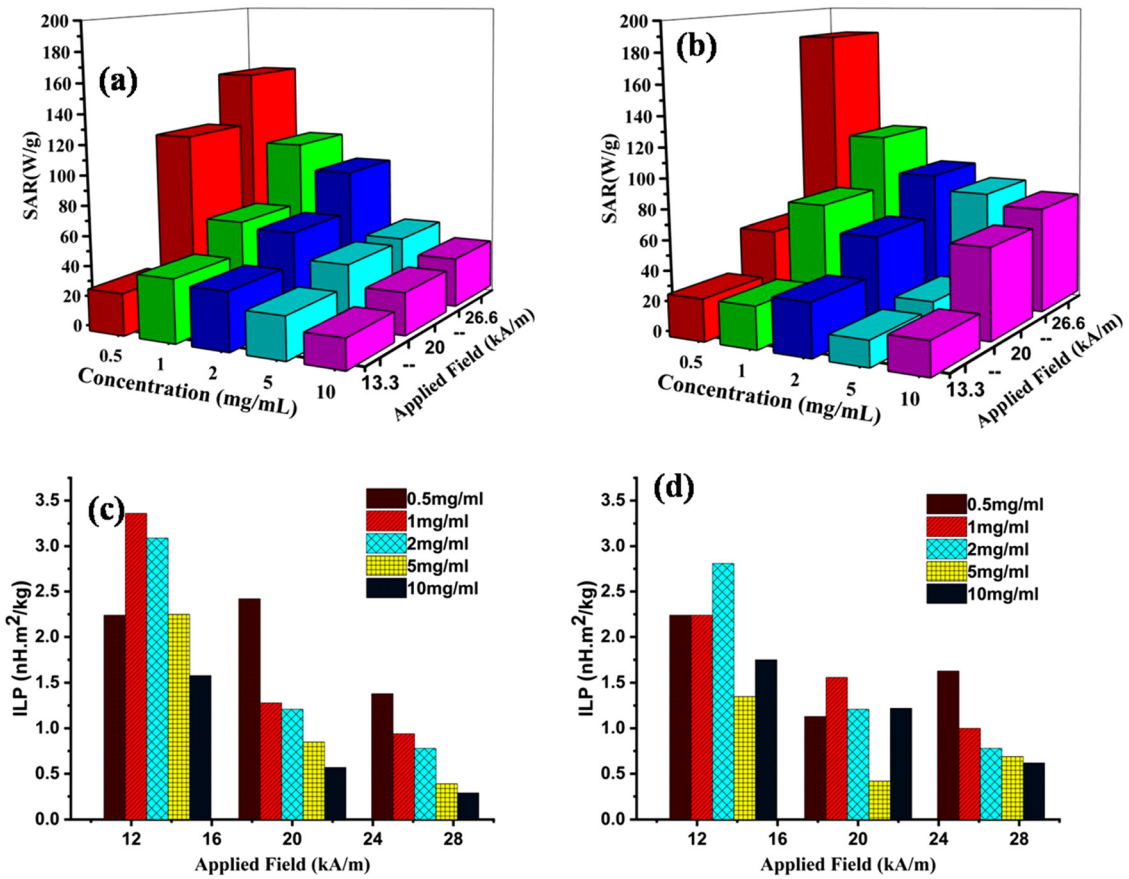

Fig. 2 The SAR values of the bare MIONPs (a) and CS–MIONPs (b), the ILP values of the bare MIONPs (c) and CS–MIONPs (d).

intensity of the AMF. Fig. 2a and 2b illustrate the increase in SAR performance for CS–MIONPs from 69.76 to 181.48 W g^{-1} and for bare nanoparticles from 33.11 to 153.56 W g^{-1}, as the field strength varied from 13.30 to 26.60 kA m^{-1}. The correlation between the SAR and the strength and intensity of the applied AC magnetic field was consistent with the findings of other suspensions following a similar procedure. It was observed that intrinsic factors like higher magnetization contributed to the increase in SAR but were not solely responsible for it. Additionally, the magneto-crystalline anisotropy energy (K_{eff}) of CS–MIONPs played a role in achieving a high SAR, with particle magnetic moments influencing the K_{eff} function. Consequently, the high magnetic moment in the current state amplified particle–particle interactions, increased exchange coupling energy, and enhanced the effectiveness of magnetic hyperthermia.

3.3 Drug loading and release

DOX's loading efficiency and capacity were studied with different pH values, as depicted in Fig. 3c. The CS–MIONPs were conjugated with the clinically-approved model anticancer agent DOX. DOX exhibits an emission spectrum at 595 nm after being excited at 480 nm, despite having a distinct absorption at 485 nm.[35] As a result, fluorescence spectroscopy was utilized in water with a pH of 7 to determine the DOX conjugation chemistry on the surfaces of CS–MIONPs (DOX@CS–MIONPs) (Fig. 3d and 3e). After chitosan coating and drug grafting, zeta potential studies were utilized to quantify the charge on the surface of CS–MIONPs. For the bare MIONPs, a positive zeta potential value was seen at pH 7.4. Zeta potential values shifted from positive to negative due to the surface charge alteration produced by CS–MIONPs with chitosan. Since the drug-protonated primary amine induces a positive charge, the cationic properties of DOX molecules are responsible for the zeta potential values which subsequently shift to the positive side. As a result, the surface charge of CS–MIONPs is altered by electrostatic interactions between the polymer and the DOX molecules. According to the calculations made using fluorescence spectra, the amount of DOX grafted onto the surface of CS–MIONPs was found to be 60.88% on 1 mg ml^{-1} of CS–MIONPs and 25.24% on 0.50 mg ml^{-1} of CS–MIONPs.

The performance of DOX release at various pH levels was examined, for instance, at pH 7.4, pH 5, and other pH levels at 37 °C. After 24 hours at pH 2.5, about 68.13% of DOX was released from nanoformulations; after the same period at pH 5.00, 7.4, and 9.00 about 56.27, 24.06, and 14.73% of drugs were released, respectively, as shown in Fig. 3c. Interestingly, the release profiles reveal increased DOX releasing rates at pH values of 2.5 and 5.0. As anticipated, after 24 hours, nanofor-

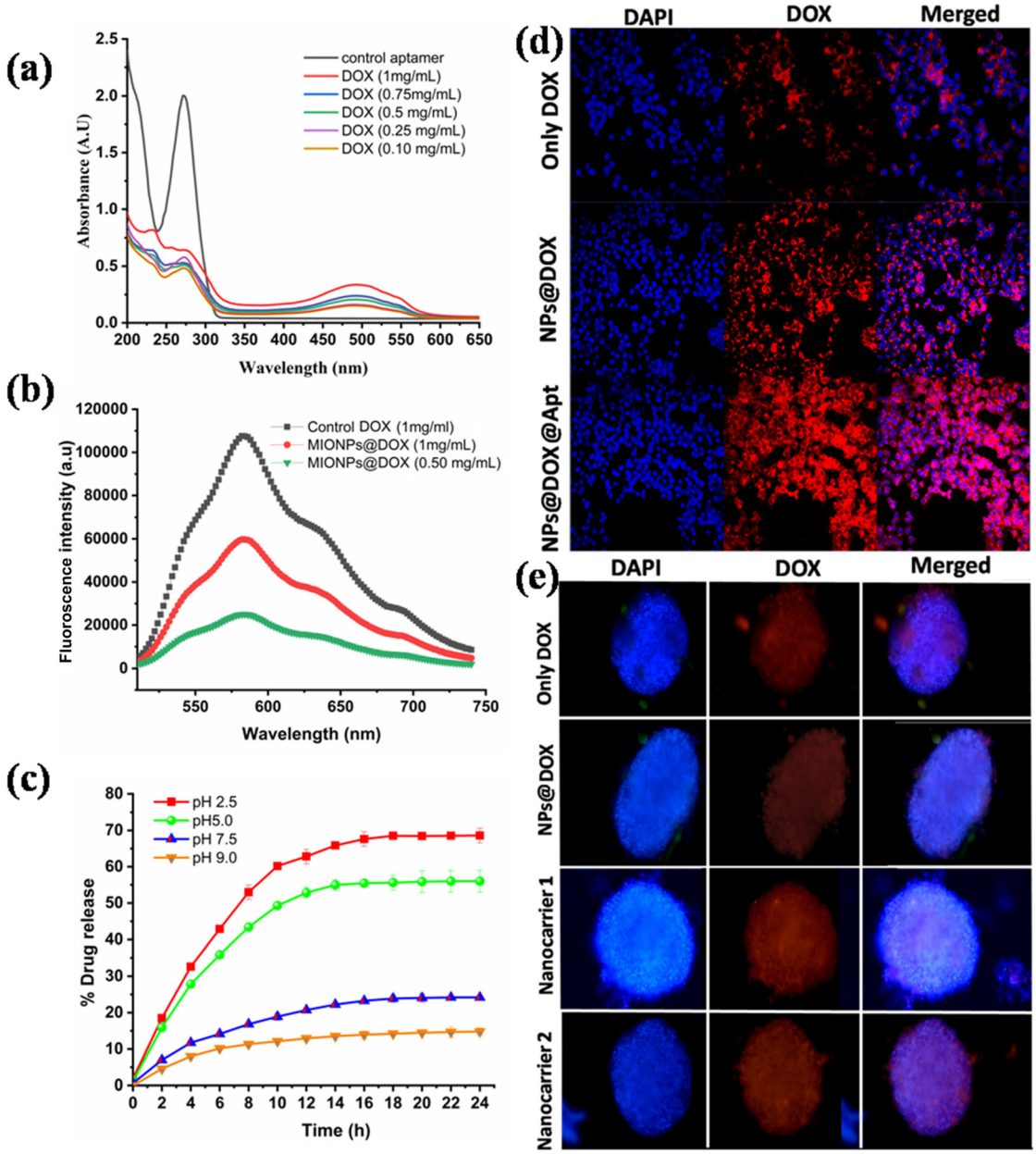

Fig. 3 DOX loading on the CS–MIONPs and release in water. (a) Fluorescence spectra of DOX and DOX@CS–MIONPs, (b and c) DOX release from DOX@CS–MIONPs at different concentrations and pH values. (d) *In vitro* DOX delivery into MCF7 cells: (i) control cells with DOX, (ii) the cells incubated with DOX@CS–MIONPs and (iii) CS–MIONPs@DOX@Apt in the 2D cell culture; (e) *in vitro* DOX delivery into MCF7 cells: cells incubated (i) control cells with DOX, (ii) with DOX@CS–MIONPs (iii) with nanocarrier 1 (DOX@CS–MIONPs) and (iv) with nanocarrier 2 (CS–MIONPs@DOX@Apt), in the 3D cell culture.

mulations produced less medication at physiological pH. Confocal microscopy (CLSM) was utilized to observe how DOX@CS–MIONPs release drugs into MCF7 cells (Fig. 3d and 3e). After 24 hours of incubation, the CLSM data showed that DOX@CS–MIONPs localized in the cellular microenvironment released DOX into the cytoplasm and entered the nucleus (Fig. 3d and e). The DOX@CS–MIONPs batch, however, had a significant amount of DOX in the cytoplasm after 24 hours of incubation (Fig. 3d and 3e). For control DOX samples, a comparable pattern was seen (shown in the figure).[10]

To avoid danger to healthy tissue, the optimal anti-tumor treatment should release its maximum amount of medicine inside or close to the tumor cells. Hence, there is a strong need for MIONPs that exhibit rapid release specifically in the targeted region and minimal release in regular sites. In order to assess the *in vitro* drug release from DOX@CS–MIONPs, we conducted experiments at four different pH values. This study is crucial for achieving selective drug delivery to the tumor site, as it minimizes premature release through circulation while ensuring adequate drug concentration to efficiently elim-

inate cancer cells once the CS–MIONPs reach the tumor site. Our hypothesis suggests that the accelerated release of DOX at low pH values, resembling the tumor microenvironment, is attributed to a reduced interface among DOX and –OH groups on the surfaces of DOX@CS–MIONPs, as well as the re-protonation of the $-NH_2$ group of DOX. It is significant to note the biphasic releasing profile of DOX with the initial phase within 6–8 hours followed by a continuous releasing phase. This controlled releasing mechanism is advantageous for cancer treatment, as this phase effectively targets and eliminates the more significant part of the cancer tumor during the initial phase. In contrast, the sustained release maintains a therapeutic drug concentration over an extended period. This approach helps in maintaining drug release within the therapeutics, prevents dose-related adverse effects, and inhibits tumor growth. Due to the current concentration gradient, drug diffusion in the eluting medium may be due to the release of DOX from DOX@CS–MIONPs.[35]

3.4 Cytotoxicity and biocompatibility analysis

The cytotoxicity and biocompatibility of CS–MIONPs were examined in both 2D and 3D cell culture models. It is essential to highlight that using a 3D culture system served as a proof-of-concept, demonstrating the effectiveness and functionality of CS–MIONPs under conditions that mimic actual tumor tissues. Numerous studies have examined the cytotoxicity of iron oxide nanoparticles in 2D cultures. However, how cells engage with 3D-structured nanomaterials in a genuine tissue milieu cannot be fully understood using a 2D culture setup.[36] MCF7 cell lines were used to assess the CS–MIONPs biocompatibility and cytotoxicity. The cytotoxicity of CS–MIONPs was assessed by incubating the cells with varying dosages of nanoparticles (10, 25, 50, 100, 200, and 400 μg mL^{-1}) and compositions (*i.e.*, CS–MIONPs, DOX@CS–MIONPs and nanocarrier, *i.e.*, Apt@DOX@CS–MIONPs) at 24 h.

As mentioned above, the MTT assay was utilized to determine the cell viability, revealing no apparent toxicity of CS–MIONPs when incubated with cells at the appropriate concentrations. However, after ten days of incubation at higher dosages, the CS–MIONPs showed discernible toxicity of the cell line (Fig. 4c and 4d). CS–MIONPs have demonstrated biocompatibility with a mild cytotoxic effect, as previously evaluated. To investigate the anticancer activity of CS–MIONPs with DOX conjugation, MCF7 cells were utilized, and the effect was examined on the concentration and time of CS–MIONPs (Fig. 4a and 4b). The cytotoxicity effect of different concentrations and compositions of nanoparticles (CS–MIONPs, DOX@CS–MIONPs, and the nanocarrier Apt@DOX@CS–MIONPs) on cell viability was assessed (Fig. 4a). According to Fig. 4a, DOX@CS–MIONPs exhibited significant cell killing, resulting in over 71.48% of cell survival in 2D culture after 24 hours. The DOX@CS–MIONP radical cell killing impact of 3D culture was studied by the concentration dependent anticancer activity profile, and within 24 hours, cell death rates of about 92.2% were noted (Fig. 4b). The data thus support the localizations of DOX in the cytoplasm following endocytosis and activation of the anticancer mechanism that leads to cautious cell death.

The cytotoxicity of CS–MIONPs and their compositions (CS–MIONPs, DOX@CS–MIONPs, and the nanocarrier DOX@CS–MIONPs@Apt) was assessed at various time points: day 0 (1 h), 2, 4, 6, 8, and day 10 after incubating the cells with CS–MIONPs. Optical microscopy images of DOX@CS–MIONPs after incubation with cells are presented in Fig. 4c. It is exciting to note that, likely due to the surface charge of DOX@CS–MIONPs, significant concentrations of them clustered near the cells. This property of DOX@CS–MIONPs, where the drug-loaded nanoparticles can release their payload locally on or near the cell surface, holds potential advantages. Fig. 4c shows the tumor volume plotted from day 1 to day 10. The accumulations of DOX@CS–MIONPs around the cells were particularly noticeable in RAW cells, likely attributed to their phagocytic characteristics. In the control group without any therapeutic drug, cell viability was 100%. However, significant cell death was observed in all analyzed samples containing pure DOX and DOX-loaded DOX@CS–MIONPs. Fig. 4d shows an optical microscope image of cells after 24 hours of incubation with DOX-loaded CS–MIONPs. Even at lower total delivered dosages, DOX@CS–MIONPs exhibit superior drug efficacy than free drugs, which is exciting but not unexpected. This could be explained by the localization of DOX@CS–MIONPs close to the cells, which results in localized drug administration to the cells. The higher efficacy of DOX-loaded CS–MIONPs compared to pure DOX is mainly due to the internalization of CS–MIONPs by cells.[35]

3.5 Synergetic magneto-chemotherapy

Given that the DOX-loaded CS–MIONPs demonstrated high magnetic moment, good biocompatibility, and anticancer effect on breast cancer cells, we focused on nanoformulations *in vitro* magneto-chemotherapy (MCT) performance in this study. Doxorubicin is a substance frequently used to treat breast cancer and has a well-established mode of action. The effectiveness of drug loading was higher due to the very moderate experimental parameters for electrostatic loading and magnetic separation. In the present study, DOX released from CS-coated MIONPs could offer human breast cancer cell lines and efficient anticancer therapy with a dual function of hyperthermia and chemotherapy. Despite being loaded onto chitosan-coated MIONPs, doxorubicin still has a charge higher than negatively or neutrally charged molecules, suggesting that it may be passing the cell membrane.[36] We looked at how well chemotherapy and thermotherapy worked together (due to DOX). In a previous section, the continuous release of DOX from DOX@CS–MIONPs on the MCF7 cell line was demonstrated (Fig. 4a). To ensure the maximum *in vitro* therapeutic efficacy of the synergistic magnetic hyperthermia-chemotherapy approach, we modified parameters such as the hyperthermia therapeutic dose and the cellular incubation time of DOX@CS–MIONPs. This was done to avoid masking the effect of the synergistic platform by cell death caused by individual therapies. An improved therapeutic anti-cancer

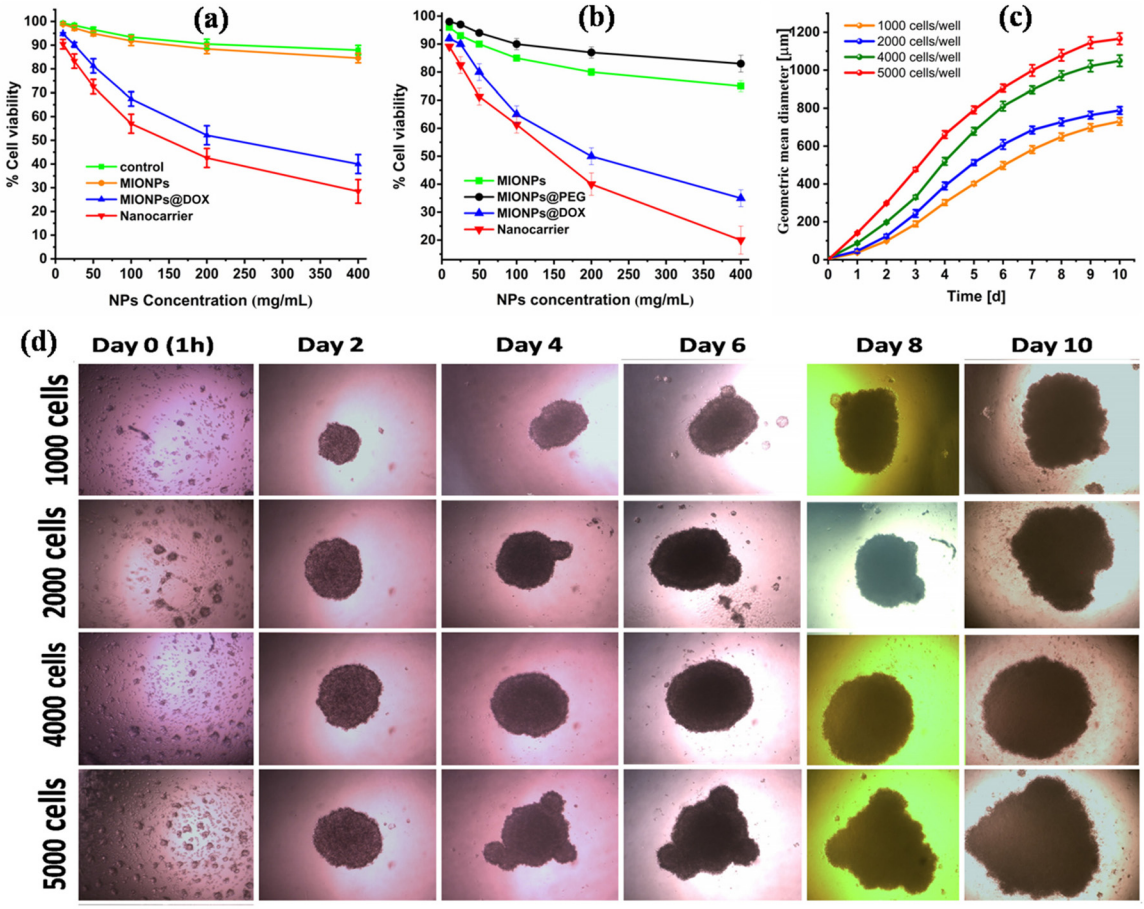

Fig. 4 (a) Concentration-dependent anticancer activity of DOX-conjugated CS–MIONPs on MCF7 cells in the 2D culture, (b) concentration-dependent anticancer activity of DOX-conjugated CS–MIONPs on MCF7 cells in the 3D culture at 24 h (c) mean spheroid diameter MCF7 cells concerning time. (d) Optical microscope image of cell activity of DOX conjugated on MCF7 cells.

impact was seen when doxorubicin loaded with CS–MIONPs was employed for hyperthermia-chemotherapy combo treatment. We evaluated the cell survival without an AMF to investigate the interaction between MCT and induced drug release. The temperature of the cellular environment, additional control samples, and suspended nanoformulations is controlled during the *in vitro* MCT to remain between 42 to 44 °C without going over the MFH threshold.[10] DOX release from a magnetically activated nanoformulation and MFH stimulation killed cancer cells. Hence, there is sufficient localized heat ablation of MFH and release of therapeutic cargo to cause cancer cell death. A well-known molecular route for self-destruction of cells in a constructed cycle is known as "apoptosis," the term for programmed cell death. To verify MCT's superiority in insisting on 'apoptosis,' the DOX@CS–MIONPs were tested with an MCF7 cell line and subjected to MCT for 30 min. The DOX@CS–MIONPs *in vitro* MCT effectiveness was assessed in 3D cell culture medium.[37] The tumor destruction was estimated in the tumor-induced 3D cell culture for 30 days of administration. After the study, it was found that MCT for 30 minutes significantly decreased the tumor volume compared to control. The location of DOX@CS–MIONPs may be indicated visually by the red area surrounding the cell tumors. While the tumor volume of DOX@CS–MIONP-treated tumors exhibited a significant decrease in MCT for 30 min compared to control, it showed a substantial increase from DOX@CS–MIONP-treated tumors. The plots shown in Fig. 5a and 5b demonstrate a noteworthy differentiation in cell viability of the control and the plain implant group, both with and without the AC magnetic field, in both 2D mono-layered and 3D spheroid cultures. Anup *et al.* focus on the progress of 3D-printed implants for adjuvant therapeutics in cancer treatment. The therapeutic potentiality of the 3D-printed implants was determined using 2D and 3D tumor models. Various assays and gene expression analyses were performed to assess the cytotoxicity, apoptosis, cell cycle, and the bio-molecular features and bio-mechanics of the implant.[38] Dhiman *et al.* studied the 3D microfluidic model based on collagen for interaction between lung carcinoma cells and mesenchymal stem cells (MSCs) treated with hyperthermia. Hyperthermia treatment of MSCs prior to co-culture with lung carcinoma cells introduces a unique variable that investigates the impact of thermally treated MSCs on tumor spheroid growth.[39] Kumeria *et al.* explored the potential application of iron oxide nanowires

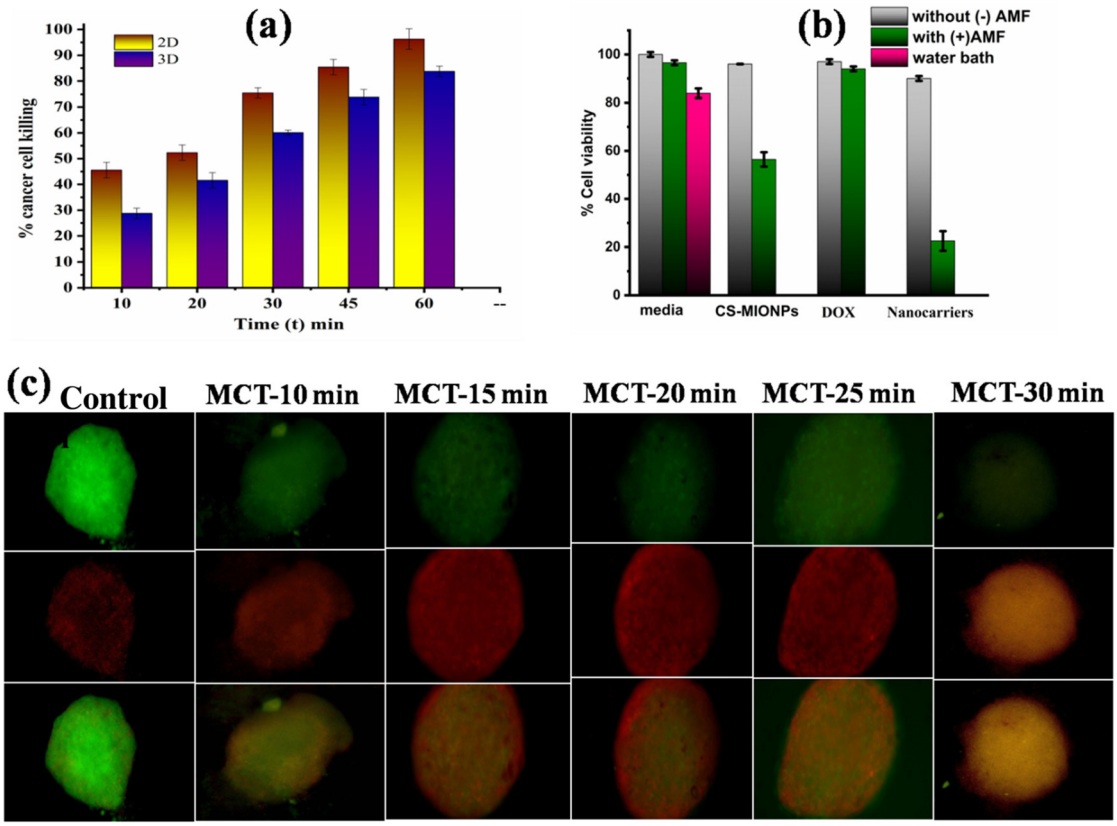

Fig. 5 (a) Cytotoxicity effects of the CS–MIONPs on 2D and 3D cell cultures with MCT, (b) the biocompatibility and cytotoxicity of the CS–MIONPs in control, CS–MIONPs, DOX@CS–MIONPs and nanocarrier *i.e.*, DOX@CS–MIONPs + Apt with and without the AMF. (c) The tumor regression study on a 3D cell model investigating the *in vitro* cancer cell killing achieved by magneto-chemotherapy (MCT) using the CS–MIONPs alone and DOX-conjugated CS–MIONPs.

extracted from biofilm waste generated by bacteria (*Mariprofundus ferrooxydans*) for cancer therapy. The *in vitro* therapeutic efficacy of Bac-FeOxNWs loaded with DOX was lower in a 3D cell culture setup than in a 2D cell culture setup. In the 3D cell culture environment, the application of AMF-induced hyperthermia using Bac-FeOxNWs resulted in a 36% decrease in cell viability for breast cancer cells after 10 minutes of exposure to the AMF.[35]

This finding implies that DOX@CS–MIONPs therapy reduced tumor growth by down-regulating the protein expression in cell cycle regulations and anti-apoptosis.[40] The data presented here confirmed that DOX@CS–MIONPs were efficiently bound and delivered to MCF-7 cells. Due to more effective internalization, DOX@CS–MIONPs also demonstrated higher cytotoxicity effects on MCF-7 cells.[17] Magneto chemotherapy can be used to treat malignant cells with superior anticancer therapeutic effects in a short amount of time. The developed drug-loaded nanoformulation used in this study demonstrated a sufficient anticancer therapeutic effect when subjected to AMF-induced hyperthermia. An optimal therapeutic dose is needed to eradicate the tumor *in vivo*. The CS–MIONPs prepared in this study feature magnetic solid moments and magnetic field-responsive nanocarriers, enabling them to deliver effective hyperthermic heating in a deliberate and controlled manner. As a result, the combinational therapeutics approach is comparatively more efficient than employing just one technique, such as chemotherapy or magnetic hyperthermia.[10]

4. Conclusions

The ability of CS–MIONPs and DOX-attached CS–MIONPs to induce tumor cell death under an AMF is demonstrated in this study, along with their drawbacks when used with MCF7 cells. The implant's *in vitro* evaluation in 3D spheroid and 2D monolayer models demonstrated the effectiveness of this hybrid strategy in treating cancer. The combination of chemotherapeutic drug release improves the potent efficiency of MHT in eliminating cancer cells. One step closer to the reality of personalized medicine may be the use of 3D models to identify innovative therapeutic methods and biomarkers.

Author contributions

Vishwajeet M. Khot and Nanasaheb D. Thorat contributed to the conception of the study; Satish S. Phalake carried out the

synthesis and characterization of the MIONPs and significantly contributed to the analysis and manuscript preparation; Syed A. M. Tofail and Sandeep B. Somvanshi helped perform constructive discussions regarding the analysis. Vishwajeet M. Khot and Nanasaheb D. Thorat provided expertise, corrected the manuscript, and helped in acquiring funding. All authors discussed the results and contributed to the final manuscript.

Conflicts of interest

The authors declare no competing financial interest.

Acknowledgements

Author VMK is thankful to the D. Y. Patil Education Society (Deemed to be University), Kolhapur for financial support through the research project (Sanction No. DYPES/DU/R&D/2021/276). Authors, SSP are gratefully thanks for to Chhatrapati Shahu Maharaj Research Training and Human Development Institute (SARTHI), Government of Maharashtra, India for awarding the Junior Research Fellowship (JRF) (Sanction No. CSMNRF-2021/2021-22/896). N. D. Thorat acknowledges funding under the Science Foundation Ireland and Irish Research Council (SFI-IRC) pathway programme (21/Q9 PATH-S/9634).

References

1 S. He, H. Zhang, Y. Liu, F. Sun, X. Yu, X. Li, L. Zhang, L. Wang, K. Mao, G. Wang, Y. Lin, Z. Han, R. Sabirianov and H. Zeng, Maximizing Specific Loss Power for Magnetic Hyperthermia by Hard–Soft Mixed Ferrites, *Small*, 2018, **14**(29), 1–9, DOI: **10.1002/smll.201800135**.

2 K. Yang, Y. Liu, Y. Liu, Q. Zhang, C. Kong, C. Yi, Z. Zhou, Z. Wang, G. Zhang, Y. Zhang, N. M. Khashab, X. Chen and Z. Nie, Cooperative Assembly of Magneto-Nanovesicles with Tunable Wall Thickness and Permeability for MRI-Guided Drug Delivery, *J. Am. Chem. Soc.*, 2018, **140**(13), 4666–4677, DOI: **10.1021/jacs.8b00884**.

3 D. Ortega and Q. A. Pankhurst, *Magnetic Hyperthermia*, 2012, vol. 1, pp. 60–88. DOI: **10.1039/9781849734844-00060**.

4 G. C. Lavorato, R. Das, Y. Xing, J. Robles, F. J. Litterst, E. Baggio-Saitovitch, M. H. Phan and H. Srikanth, Origin and Shell-Driven Optimization of the Heating Power in Core/Shell Bimagnetic Nanoparticles, *ACS Appl. Nano Mater.*, 2020, **3**(2), 1755–1765, DOI: **10.1021/acsanm.9b02449**.

5 American Cancer Society, I. 2023-Cancer-Facts-and-Figures, 2023.

6 Y. Qu, J. Li, J. Ren, J. Leng, C. Lin and D. Shi, Enhanced Magnetic Fluid Hyperthermia by Micellar Magnetic, *ACS Appl. Mater. Interfaces*, 2014, **6**(19), 16867–16879, DOI: **10.1021/am5042934**.

7 S. Jeon, B. C. Park, S. Lim, H. Y. Yoon, Y. S. Jeon, B. S. Kim, Y. K. Kim and K. Kim, Heat-Generating Iron Oxide Multigranule Nanoclusters for Enhancing Hyperthermic Efficacy in Tumor Treatment, *ACS Appl. Mater. Interfaces*, 2020, **12**(30), 33483–33491, DOI: **10.1021/acsami.0c07419**.

8 Y. J. Wang, Current Status of Superparamagnetic Iron Oxide Contrast Agents for Liver Magnetic Resonance Imaging, *World J. Gastroenterol.*, 2015, **21**(47), 13400–13402, DOI: **10.1007/BF02678498**.

9 S. Tan, Â. A. Brisson, Â. V. Dupuis, O. O. Sandre, S. Miraux, E. Thiaudi and S. E. T. Al, Doxorubicin Loaded Magnetic Polymersomes: Theranostic Nanocarriers for MR Imaging and Magneto-Chemotherapy, *ACS Nano*, 2011, **5**(2), 1122–1140.

10 A. Salunkhe, V. Khot, S. I. Patil, S. A. M. Tofail, J. Bauer and N. D. Thorat, MRI Guided Magneto-Chemotherapy with High-Magnetic-Moment Iron Oxide Nanoparticles for Cancer Theranostics, *ACS Appl. Bio Mater.*, 2020, **3**(4), 2305–2313, DOI: **10.1021/acsabm.0c00077**.

11 L. Beola, L. Asín, R. M. Fratila, V. Herrero, J. M. De La Fuente, V. Grazú and L. Gutiérrez, Dual Role of Magnetic Nanoparticles as Intracellular Hotspots and Extracellular Matrix Disruptors Triggered by Magnetic Hyperthermia in 3D Cell Culture Models, *ACS Appl. Mater. Interfaces*, 2018, **10**(51), 44301–44313, DOI: **10.1021/acsami.8b18270**.

12 M. K. Kim, B. G. Cha and J. Kim, Directed Assembly of Magnetic Nanoparticles into Centimeter Scale Wires for a 3D Cell Culture Platform, *Chem. Mater.*, 2022, **34**(10), 4437–4445, DOI: **10.1021/acs.chemmater.2c00120**.

13 K. Simeonidis, C. Martinez-Boubeta, D. Serantes, S. Ruta, O. Chubykalo-Fesenko, R. Chantrell, J. Oró-Solé, L. Balcells, A. S. Kamzin, R. A. Nazipov, A. Makridis and M. Angelakeris, Controlling Magnetization Reversal and Hyperthermia Efficiency in Core-Shell Iron-Iron Oxide Magnetic Nanoparticles by Tuning the Interphase Coupling, *ACS Appl. Nano Mater.*, 2020, **3**(5), 4465–4476, DOI: **10.1021/acsanm.0c00568**.

14 J. Li, Q. Li, M. He, F. Ding, L. Cai, M. Zhao, L. Dong, Q. Wang and K. Xu, AS1411 Aptamer-Modified Theranostic Liposomes Co-Encapsulating Manganese Oxide Nano-Contrast Agent and Paclitaxel for MRI and Therapy of Cancer, *RSC Adv.*, 2019, **9**(60), 34837–34846, DOI: **10.1039/c9ra06878c**.

15 X. Sun, B. Liu, X. Chen, H. Lin, Y. Peng, Y. Li, H. Zheng, Y. Xu, X. Ou, S. Yan, Z. Wu, S. Deng, L. Zhang and P. Zhao, Aptamer-Assisted Superparamagnetic Iron Oxide Nanoparticles as Multifunctional Drug Delivery Platform for Chemo-Photodynamic Combination Therapy, *J. Mater. Sci. Mater. Med.*, 2019, **30**(7), 1–15, DOI: **10.1007/s10856-019-6278-y**.

16 H. Alijani, A. Noori, N. Faridi, S. Z. Bathaie and M. F. Mousavi, Aptamer-Functionalized Fe_3O_4@MOF Nanocarrier for Targeted Drug Delivery and Fluorescence Imaging of the Triple-Negative MDA-MB-231 Breast Cancer Cells, *J. Solid State Chem.*, 2020, **292**, 121680, DOI: **10.1016/j.jssc.2020.121680**.

17 X. Han, Y. Jiang, S. Li, Y. Zhang, X. Ma, Z. Wu, Z. Wu and X. Qi, Multivalent Aptamer-Modified Tetrahedral DNA Nanocage Demonstrates High Selectivity and Safety for Anti-Tumor Therapy, *Nanoscale*, 2019, **11**(1), 339–347, DOI: **10.1039/c8nr05546g**.

18 S. S. Phalake, M. S. Lad, K. V. Kadam, S. A. M. Tofail, N. D. Thorat and V. M. Khot, Application of $Mn_xFe_{1-x}Fe_2O_4$ (x = 0–1) Nanoparticles in Magnetic Fluid Hyperthermia: Correlation with Cation Distribution and Magnetostructural Properties, *ACS Omega*, 2022, **7**(48), 44187–44198, DOI: **10.1021/acsomega.2c05651**.

19 G. Deng, H. Zha, H. Luo and Y. Zhou, Aptamer-Conjugated Gold Nanoparticles and Their Diagnostic and Therapeutic Roles in Cancer, *Front. Bioeng. Biotechnol.*, 2023, **11**, 1–15, DOI: **10.3389/fbioe.2023.1118546**.

20 D. Bharathi, R. Ranjithkumar, S. Vasantharaj, B. Chandarshekar and V. Bhuvaneshwari, Synthesis and Characterization of Chitosan/Iron Oxide Nanocomposite for Biomedical Applications, *Int. J. Biol. Macromol.*, 2019, **132**, 880–887, DOI: **10.1016/j.ijbiomac.2019.03.233**.

21 B. Sanz, R. Cabreira-Gomes, T. E. Torres, D. P. Valdés, E. Lima, E. De Biasi, R. D. Zysler, M. R. Ibarra and G. F. Goya, Low-Dimensional Assemblies of Magnetic $MnFe_2O_4$ Nanoparticles and Direct in Vitro Measurements of Enhanced Heating Driven by Dipolar Interactions: Implications for Magnetic Hyperthermia, *ACS Appl. Nano Mater.*, 2020, **3**(9), 8719–8731, DOI: **10.1021/acsanm.0c01545**.

22 W. B. Mdlalose, S. R. Mokhosi, S. Dlamini, T. Moyo and M. Singh, Effect of Chitosan Coating on the Structural and Magnetic Properties of $MnFe_2O_4$ and $Mn_{0.5}Co_{0.5}Fe_2O_4$ Nanoparticles, *AIP Adv.*, 2018, **8**(5), 056726, DOI: **10.1063/1.5007760**.

23 A. Ereath Beeran, S. S. Nazeer, F. B. Fernandez, K. S. Muvvala, W. Wunderlich, S. Anil, S. Vellappally, M. S. Ramachandra Rao, A. John, R. S. Jayasree and P. R. Harikrishna Varma, An Aqueous Method for the Controlled Manganese (Mn^{2+}) Substitution in Superparamagnetic Iron Oxide Nanoparticles for Contrast Enhancement in MRI, *Phys. Chem. Chem. Phys.*, 2015, **17**(6), 4609–4619, DOI: **10.1039/c4cp05122j**.

24 P. Hugounenq, M. Levy, D. Alloyeau, L. Lartigue, E. Dubois, V. Cabuil, C. Ricolleau, S. Roux, C. Wilhelm, F. Gazeau and R. Bazzi, Iron Oxide Monocrystalline Nanoflowers for Highly Efficient Magnetic Hyperthermia, *J. Phys. Chem. C*, 2012, **116**(29), 15702–15712, DOI: **10.1021/jp3025478**.

25 P. B. Shete, R. M. Patil, N. D. Thorat, A. Prasad, R. S. Ningthoujam, S. J. Ghosh and S. H. Pawar, Magnetic Chitosan Nanocomposite for Hyperthermia Therapy Application: Preparation, Characterization and in Vitro Experiments, *Appl. Surf. Sci.*, 2014, **288**, 149–157, DOI: **10.1016/j.apsusc.2013.09.169**.

26 M. F. Tsai, C. Hsu, C. S. Yeh, Y. J. Hsiao, C. H. Su and L. F. Wang, Tuning the Distance of Rattle-Shaped IONP@Shell-in-Shell Nanoparticles for Magnetically-Targeted Photothermal Therapy in the Second Near-Infrared Window, *ACS Appl. Mater. Interfaces*, 2018, **10**(2), 1508–1519, DOI: **10.1021/acsami.7b14593**.

27 A. Konwar, S. Kalita, J. Kotoky and D. Chowdhury, Chitosan-Iron Oxide Coated Graphene Oxide Nanocomposite Hydrogel: A Robust and Soft Antimicrobial Biofilm, *ACS Appl. Mater. Interfaces*, 2016, **8**(32), 20625–20634, DOI: **10.1021/acsami.6b07510**.

28 V. Zamora-Mora, M. Fernández-Gutiérrez, Á. González-Gómez, B. Sanz, J. S. Román, G. F. Goya, R. Hernández and C. Mijangos, Chitosan Nanoparticles for Combined Drug Delivery and Magnetic Hyperthermia: From Preparation to in Vitro Studies, *Carbohydr. Polym.*, 2017, **157**, 361–370, DOI: **10.1016/j.carbpol.2016.09.084**.

29 A. Hervault and N. T. K. Thanh, Magnetic nanoparticle-based therapeutic agents for thermo-chemotherapy treatment of cancer, *Nanoscale*, 2014, **6**(20), 11553–11573, DOI: **10.1039/c4nr03482a**.

30 I. Castellanos-Rubio, I. Rodrigo, A. Olazagoitia-Garmendia, O. Arriortua, I. Gil De Muro, J. S. Garitaonandia, J. R. Bilbao, M. L. Fdez-Gubieda, F. Plazaola, I. Orue, A. Castellanos-Rubio and M. Insausti, Highly Reproducible Hyperthermia Response in Water, Agar, and Cellular Environment by Discretely PEGylated Magnetite Nanoparticles, *ACS Appl. Mater. Interfaces*, 2020, **12**(25), 27917–27929, DOI: **10.1021/acsami.0c03222**.

31 L. Del Bianco, F. Spizzo, G. Barucca, M. R. Ruggiero, S. Geninatti Crich, M. Forzan, E. Sieni and P. Sgarbossa, Mechanism of Magnetic Heating in Mn-Doped Magnetite Nanoparticles and the Role of Intertwined Structural and Magnetic Properties, *Nanoscale*, 2019, **11**(22), 10896–10910, DOI: **10.1039/c9nr03131f**.

32 A. Doaga, A. M. Cojocariu, W. Amin, F. Heib, P. Bender, R. Hempelmann and O. F. Caltun, Synthesis and Characterizations of Manganese Ferrites for Hyperthermia Applications, *Mater. Chem. Phys.*, 2013, **143**(1), 305–310, DOI: **10.1016/j.matchemphys.2013.08.066**.

33 P. H. Nam, N. X. Phuc, D. H. Manh, D. K. Tung, V. Q. Nguyen, N. H. Nam, P. K. Son, T. N. Bach and P. T. Phong, Physical Characterization and Heating Efficacy of Chitosan-Coated Cobalt Ferrite Nanoparticles for Hyperthermia Application, *Phys. E*, 2021, **134**, 114862, DOI: **10.1016/j.physe.2021.114862**.

34 Y. Oh, N. Lee, H. W. Kang and J. Oh, In Vitro Study on Apoptotic Cell Death by Effective Magnetic Hyperthermia with Chitosan-Coated $MnFe_2O_4$, *Nanotechnology*, 2016, **27**(11), 115101, DOI: **10.1088/0957-4484/27/11/115101**.

35 T. Kumeria, S. Maher, Y. Wang, G. Kaur, L. Wang, M. Erkelens, P. Forward, M. F. Lambert, A. Evdokiou and D. Losic, Naturally Derived Iron Oxide Nanowires from Bacteria for Magnetically Triggered Drug Release and Cancer Hyperthermia in 2D and 3D Culture Environments: Bacteria Biofilm to Potent Cancer Therapeutic, *Biomacromolecules*, 2016, **17**(8), 2726–2736, DOI: **10.1021/acs.biomac.6b00786**.

36 V. Kulkarni, D. Bodas and K. Paknikar, Assessment of an Integrative Anticancer Treatment Using an in Vitro

Perfusion-Enabled 3D Breast Tumor Model, *ACS Biomater. Sci. Eng.*, 2018, **4**(4), 1407–1417, DOI: **10.1021/acsbiomaterials.8b00153**.

37 A. T. Guduru, N. Manav, A. Mansuri, I. Gupta, D. Bhatia, A. Kumar and S. V. Dalvi, NIR-Active Porphyrin-Decorated Lipid Microbubbles for Enhanced Therapeutic Activity Enabled by Photodynamic Effect and Ultrasound in 3D Tumor Models of Breast Cancer Cell Line and Zebrafish Larvae, *ACS Appl. Bio Mater.*, 2022, **5**(9), 4270–4283, DOI: **10.1021/acsabm.2c00483**.

38 N. Anup, A. Gadeval and R. K. Tekade, A 3D-Printed Graphene BioFuse Implant for Postsurgical Adjuvant Therapy of Cancer: Proof of Concept in 2D- and 3D-Spheroid Tumor Models, *ACS Appl. Bio Mater.*, 2023, **6**(3), 1195–1212, DOI: **10.1021/acsabm.2c01031**.

39 N. Dhiman, N. Shagaghi, M. Bhave, H. Sumer, P. Kingshott and S. N. Rath, Indirect Co-Culture of Lung Carcinoma Cells with Hyperthermia-Treated Mesenchymal Stem Cells Influences Tumor Spheroid Growth in a Collagen-Based 3-Dimensional Microfluidic Model, *Cytotherapy*, 2021, **23**(1), 25–36, DOI: **10.1016/j.jcyt.2020.07.004**.

40 L. R. Jaidev, D. R. Chellappan, D. V. Bhavsar, R. Ranganathan, B. Sivanantham, A. Subramanian, U. Sharma, N. R. Jagannathan, U. M. Krishnan and S. Sethuraman, Multi-Functional Nanoparticles as Theranostic Agents for the Treatment & Imaging of Pancreatic Cancer, *Acta Biomater.*, 2017, **49**, 422–433, DOI: **10.1016/j.actbio.2016.11.053**.